Journal of Alloys and Compounds 1047 (2025) 185078

Contents lists available at ScienceDirect

Journal of Alloys and Compounds

journal homepage: www.elsevier.com/locate/jalcom

Enhanced incorporation of indium in AlInN films by atmospheric-pressure metal-organic chemical vapor deposition

Shaosheng Fan [a,b], Yang Mei [a], Masao Ikeda [b,c,*], Zongliang Liu [b], Ke Xu [b,c], Leiying Ying [a], Baoping Zhang [a,d,**]

[a] Laboratory of Micro/Nano-Optoelectronics, School of Electronic Science and Engineering, Xiamen University, Xiamen 361005, PR China
[b] Jiangsu Institute of Advanced Semiconductors, Suzhou, Jiangsu 215125, PR China
[c] Suzhou Institute of Nano-Tech and Nano-Bionics, Chinese Academy of Sciences (CAS), Suzhou 215123, PR China
[d] Institute of Nanoscience and Applications & College of Semiconductors, Southern University of Science and Technology, Shenzhen 518055, PR China

ARTICLE INFO

Keywords:
AlInN
MOCVD
Indium incorporation
Crystalline quality

ABSTRACT

AlInN films are attracting much attention for their applications in advanced optoelectronic and electronic devices. It is important to make clear the incorporation behavior of indium atoms during the growth of AlInN by commonly used metal organic chemical vapor deposition (MOCVD). In this paper, it is demonstrated that a higher indium incorporation is expected in atmospheric pressure growth than conventional low-pressure growth. Then, the incorporation behavior of indium in AlInN films grown by atmospheric pressure MOCVD was systematically investigated. Under atmospheric MOCVD, the indium desorption is found to play a dominant role rather than thermal decomposition as typically observed at low pressures. This distinction is attributed to the accelerated mass transport and modified adsorption-desorption dynamics under atmospheric pressure. Furthermore, increasing the NH_3 and TMI flux was found to promote the smooth surface morphology. On the other hand, increasing TMA flux led to surface degradation, which may be related to the increased growth rate with higher TMA flux. However, by simultaneously increasing the NH_3 flow rate to provide sufficient reactive N atoms, this surface degradation issue can be resolved. Based on above results, the In-incorporation behavior in AlInN under atmospheric pressure was elucidated, achieving a high indium incorporation efficiency and enabling the growth of high-quality AlInN films with smooth surface morphology simultaneously.

1. Introduction

Group III nitride semiconductors are widely used in a great many practical optoelectronic devices, such as light-emitting diodes and lasers, and power electronic devices. $Al_{0.83}In_{0.17}N$ ternary alloy, which is lattice-matched to GaN, is of essential importance in various applications including crack-free distributed Bragg reflectors (DBRs) in vertical-cavity surface-emitting lasers (VCSEL) [1,2], high-quality active region in light-emitting devices [3], and sacrificial layers [4,5] in selective wet electrochemical etching for the fabrication of advanced optoelectronic structures.

However, the growth of high-quality AlInN films remains challenging. The main difficulties arise from several factors: as the two end members of the group III-nitride system, AlN and InN exhibit significant immiscibility due to their large differences in bond strength and cation size. This immiscibility leads to severe phase separation [6,7], complicating the incorporation behavior of indium and making it difficult to grow high-quality AlInN. Secondly, the mismatch in the bond energies and the growth temperature between AlN and InN results in a rather small window of optimal growth temperature for AlInN [8]. The growth temperature of AlInN must be kept low enough to ensure the desired indium composition (~17 % for lattice-matched to GaN template), which contradicts the higher growth temperatures required to enhance the diffusion of adatoms, thereby improving crystalline quality and obtaining a smooth surface. On the other hand, it has been shown that significant enhancement of In incorporation efficiency could be achieved by growth under atmospheric pressure [9]. However, the intensifying parasitic reactions between the TMA and NH_3 with increasing

* Corresponding author at: Jiangsu Institute of Advanced Semiconductors, Suzhou, Jiangsu 215125, PR China.
** Corresponding author at: Laboratory of Micro/Nano-Optoelectronics, School of Electronic Science and Engineering, Xiamen University, Xiamen 361005, PR China.
E-mail addresses: mikeda2013@sinano.ac.cn (M. Ikeda), bzhang@xmu.edu.cn (B. Zhang).

https://doi.org/10.1016/j.jallcom.2025.185078
Received 22 September 2025; Received in revised form 27 October 2025; Accepted 16 November 2025
Available online 20 November 2025

pressure hinder the realization of high crystalline quality [10]. As a result of these conflicting constraints, almost all of the research on the MOCVD growth of AlInN has predominantly focused on low-pressure conditions [11–13]. In our prior study [14], severe parasitic reactions under atmospheric pressure were effectively suppressed through a large total gas flow rate of 72 slm and an optimized distribution among the three inlets. Consequently, the AlInN films grown under atmospheric pressure exhibit a smooth surface and a much lower density of V-pits compared with AlInN grown under low pressure. Despite of these progress, the growth behavior of AlInN under atmospheric-pressure MOCVD is still not fully understood. In this work, the growth behavior of AlInN films is further investigated. Particularly, indium incorporation behavior under varying precursor flow rates was investigated and found to follow the Langmuir model, revealing that In desorption plays a critical role in AlInN growth under atmospheric pressure.

2. Experiment and method

Epitaxial growth of AlInN ternary film has been carried out by a horizontal flow TNSC MOCVD system using a GaN template with (0001)-oriented sapphire substrate under nominal atmospheric pressure. Prior to the growth of AlInN films, these GaN templates were heated in a hydrogen-ammonia ambient from room temperature to a setpoint of 950 ℃ (ramping rate of 1 ℃/s) with a holding time of 10 mins to clean the surface, and then individually overgrown with about 1 μm thick GaN re-growth layer to bury any surface damage. Subsequently, AlInN films were deposited using trimethylaluminum (TMA), trimethylindium (TMI), and ammonia (NH_3) as Al, In, and N precursors, and nitrogen as the carrier and diluent gas. The total gas flow rate was fixed at 72 slm. The growth temperature T_g, being varied between 802 and 875 ℃, is the surface temperature of GaN as measured by the temperature-dependent thermal etching rates of GaN in H_2 + NH_3 gas flow [15], and the heater power losses due to the high flow rate gas of H_2 + NH_3 and N_2 + NH_3, assuming that the temperature difference between the thermocouple and the surface is proportional to the heater power loss due to the high flow rate gas stream when keeping the same thermocouple temperature. The setting thermocouple temperature was 8–21 ℃ higher in N_2 + NH_3 gas flow than the surface temperature T_g in the studied range. Other detailed growth parameters are described in each corresponding section. In our MOCVD reactor, although the exhaust of reactor was kept at atmospheric pressure, the pressure inside the reactor became ~50 Torr higher due to the high flow rate of N_2 carrier gas used. For ease of explanation in subsequent sections, all references to atmospheric pressure hereafter actually refer to near-atmospheric pressure (~810 Torr).

The surface morphology of AlInN epilayers was characterized by atomic force microscopy (AFM) of Bruker Dimension ICON and scanning electron microscope (SEM) of HITACHI S-4800. Quoted surface roughness (root mean square) is determined from AFM scan near the center of 2-inch wafer and averaged from three scans of the same size. Indium compositions were determined using the 2θ-ω scan of (0002) in the triple-axis mode on a Bruker D8 Discover high-resolution X-ray diffraction (HRXRD) and confirmed by EDX mapping. The thicknesses of AlInN layers were determined by cross-sectional SEM observations and calibrated by cross-sectional TEM. The growth rate was estimated by the measured thickness according to the growth time. For a microstructural analysis of the AlInN/GaN interface, TEM has been carried out for high-angle annular dark field (HAADF) measurements and energy dispersive X-ray spectroscopy (EDX) at an acceleration voltage of 300 kV in a Thermo Scientific (FEI) Themis Z. The preparation of the lamella was done using focused ion beam milling. All X-ray photoelectron spectroscopy (XPS) measurements are performed on the Thermo Fisher Scientific ESCALAB Xi+ system with the base pressure of 7.5×10^{-11} Torr during spectra acquisition. Monochromatic Al Kα radiation (1486.6 eV) was employed as the X-ray excitation source, and all spectra were collected at an angle of 54° relative to the surface normal. The XPS analysis area is approximately ϕ = 500 μm.

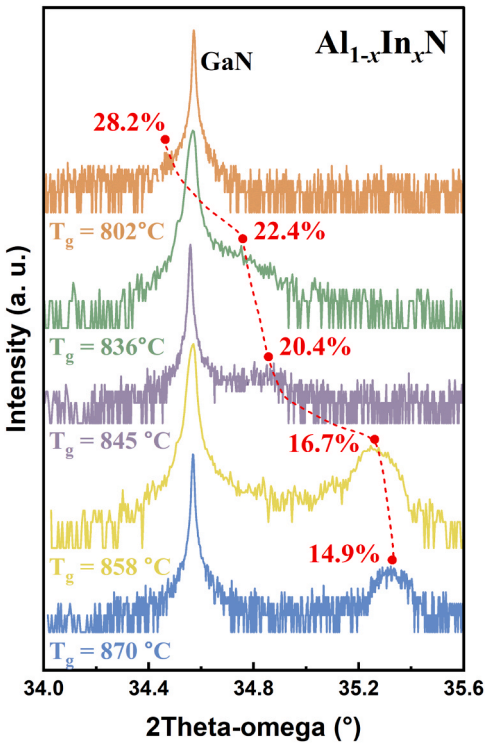

Fig. 1. The 2θ-ω HR-XRD curves around the (0002) plane of $Al_{1-x}In_xN$ ternary alloy dependent on growth temperature under atmospheric pressure.

3. Results and discussion

3.1. Effect of growth pressure on In incorporation

Fig. 1 shows the 2θ –ω scan around the (0002) plane of the $Al_{1-x}In_xN$ ternary layer grown at different growth temperatures under atmospheric pressure. Two dominant diffraction peaks were revealed from both the GaN and $Al_{1-x}In_xN$ layers, although AlInN is only a few tens of nanometers thick. As the growth temperature increased from 802 to 870 °C, the diffraction peaks of $Al_{1-x}In_xN$ tended to shift toward higher angles, indicating a decrease in the In composition.

The comparative analysis of indium composition is presented for AlInN grown under low pressure [8,11] and atmospheric pressure, as depicted in Fig. 2(a). It should be noted that the indium composition is simultaneously affected by TMI, TMA, and NH_3 for AlInN growth. To clarify the influence of pressure on indium composition, the effect of precursor flow rates (e.g., [NH_3]/[TMI+TMA]) should be excluded. As shown in Fig. 2(a), AlInN layers were grown with V/III ratios of 5600 (Sadler), 10,000 (Chung), and 2800 (this work). However, the In composition shows almost no variation (< 1 %) when the V/III ratio increases from 2800 to 9200 as shown in Fig. S1 (supplementary materials). This obviously can't explain the larger difference in In composition at the same growth temperature observed in Fig. 2(a). Hence, the growth pressure is identified as the primary factor leading to the significant variation of In composition observed in Fig. 2(a). In addition, it is observed that as the temperature increases, the In composition decreases linearly at a slope of 0.25 %, 0.24 % for low pressure, compared to 0.2 % for atmospheric pressure. And the *a*-lattice matched with the GaN buffer layer is achieved at temperatures of 790 °C, 801 °C for low pressure, and a much higher 857 °C under atmospheric pressure, indicating that the higher In incorporation efficiency is achieved under atmospheric pressure.

The Arrhenius plot is a commonly used chart for analyzing various

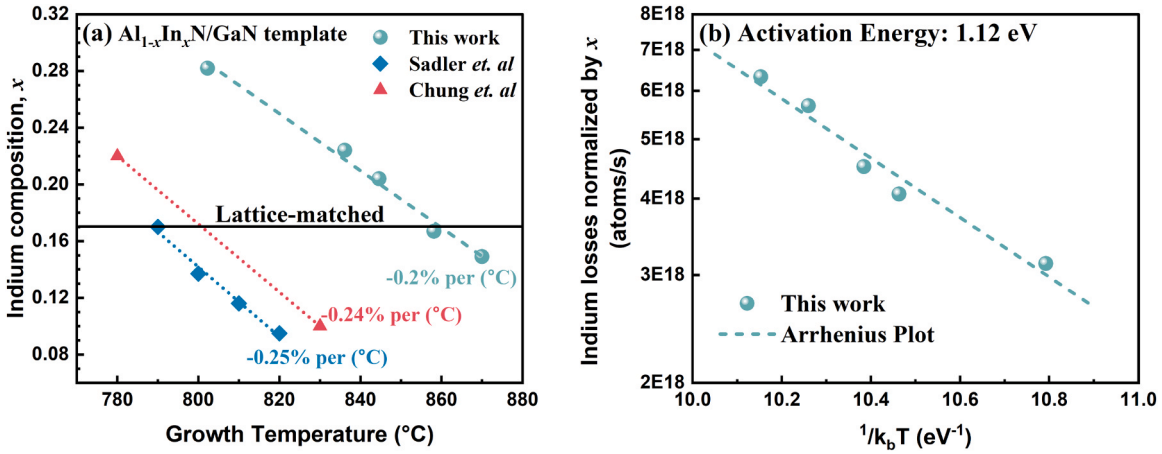

Fig. 2. (a) The growth temperature dependence of In composition in AlInN films grown under low-pressure (red triangles and blue diamonds) and atmospheric pressure (green circles). The flow rates of TMA, TMI, and NH_3 were fixed at 27.0×10^{-6}, 98.6×10^{-6}, and 0.357 mol/min under atmospheric pressure case; (b) Arrhenius plot of the indium losses normalized by In composition for AlInN grown under atmospheric pressure.

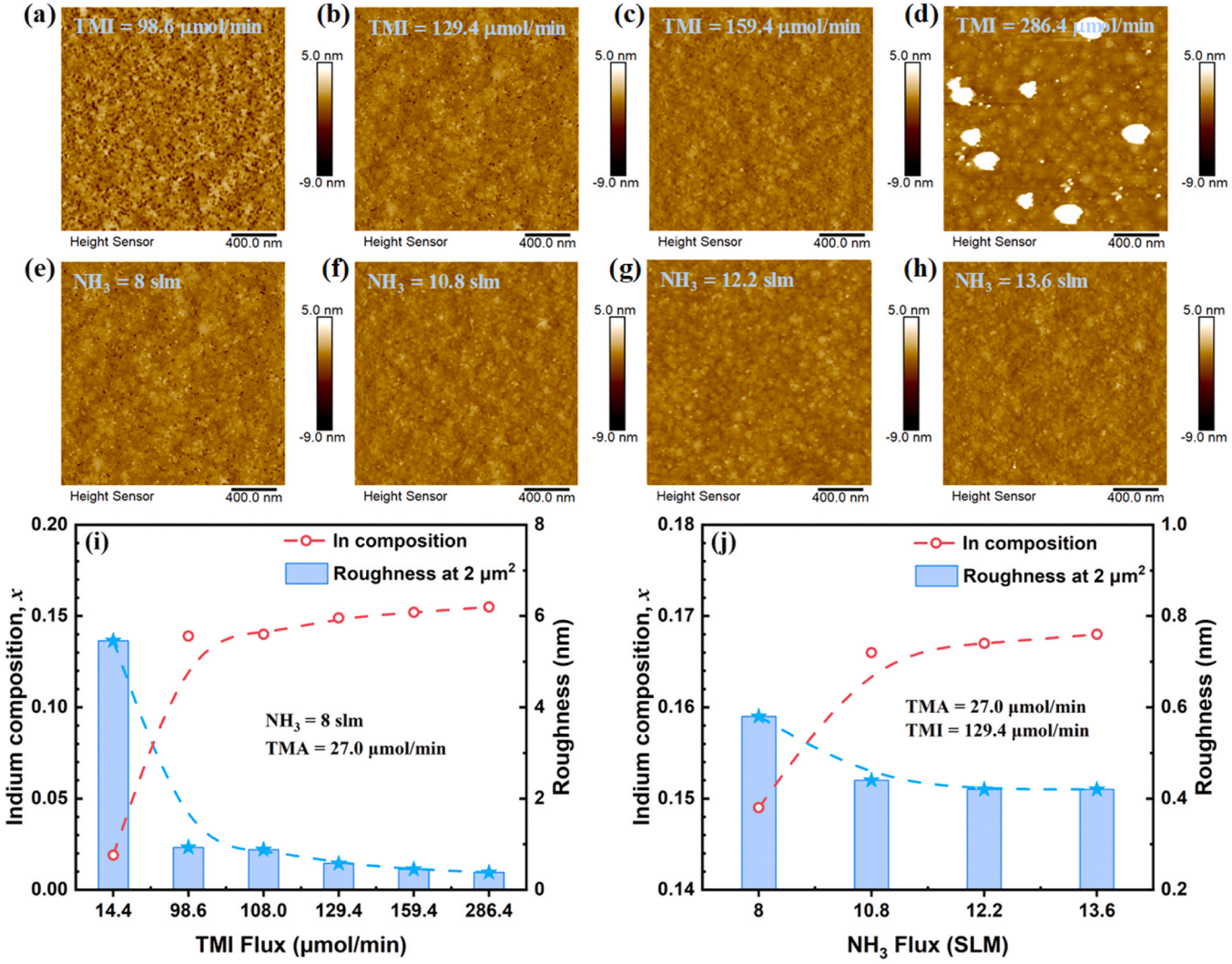

Fig. 3. The typical 2×2 μm^2 AFM image for the selected TMI flux and NH_3 flux as shown in (a - d) and (e - h); The indium composition (open circles) and surface roughness (filled stars) as a function of (i) TMI at fixed NH_3 of 8 slm and TMA of 27.0 µmol/min and (j) NH_3 flux at fixed TMI of 129.4 µmol/min and TMA of 27.0 µmol/min. All samples were grown at a growth temperature of 870 °C.

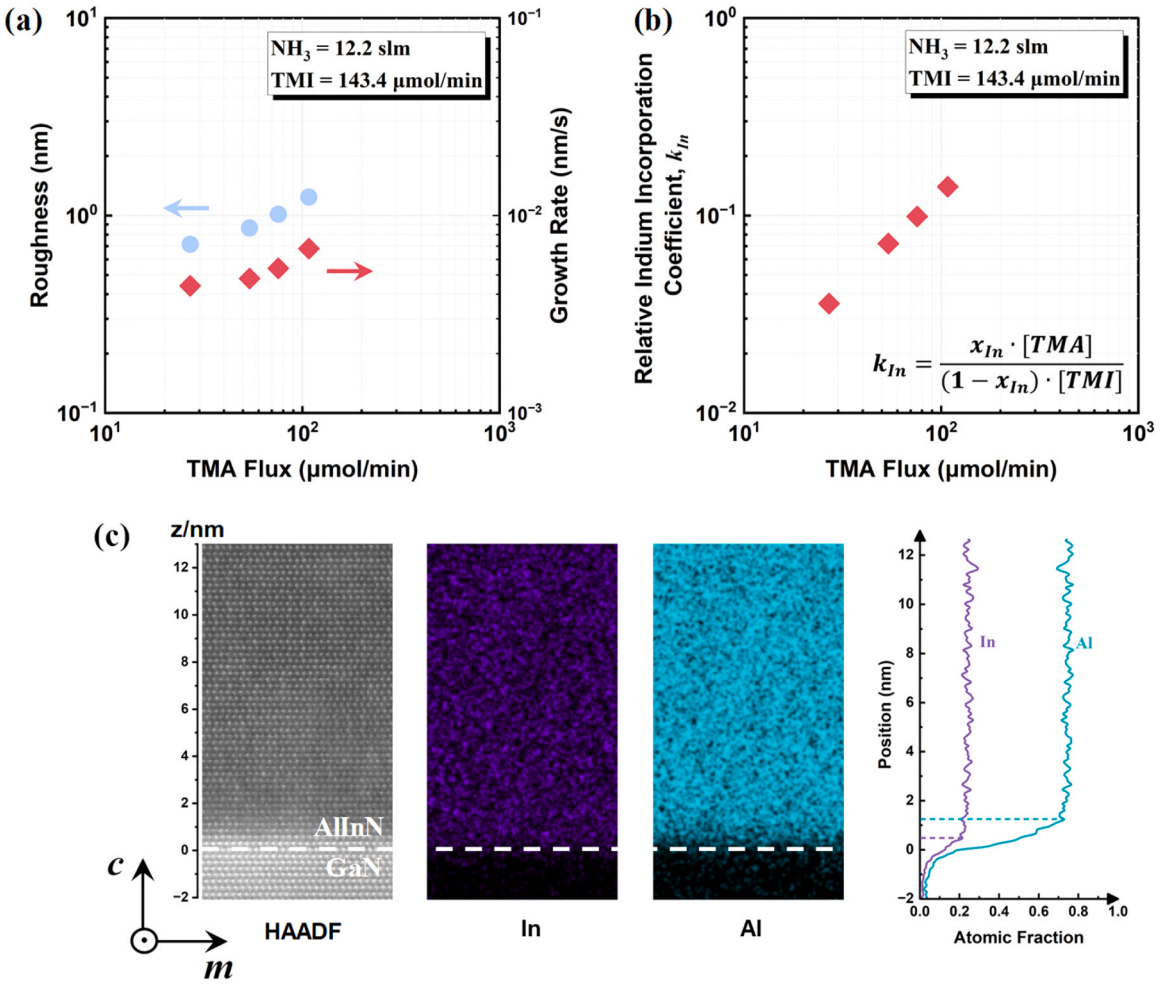

Fig. 4. The TMA flux dependence of (a) roughness (blue circles, originating from 5 × 5 μm^2 AFM image) and growth rate (red diamonds), and (b) relative indium incorporation coefficient at a fixed NH_3 of 12.2 slm, TMI of 143.4 μmol/min, and a growth temperature of 875 °C; (c) HAADF image and EDS line mapping of aluminum and indium across the AlInN/GaN interface in projection of the crystallographic *a*-axis.

thermal activation kinetics. It has been demonstrated that the amount of indium loss ($[TMI]^{loss}$) due to thermal effects is proportional to the Boltzmann factor with the activation energy (E_a) [16]:

$$[TMI]^{loss} = A \bullet x_{In} \bullet \exp\left(-\frac{E_a}{k_b T}\right) \quad (1)$$

Where A is a constant factor and x_{In} represents the In composition. $[TMI]^{loss}$ is the difference between the supplied TMI flux, *[TMI]*, and the actual indium used for the epitaxial growth ($[TMI]^{act}$), as defined by HRXRD data: $[TMI]^{act} = x_{In} \bullet [TMA]/(1 - x_{In})$. As shown in the coordinate scale, log vs. 1/eV, of Fig. 2(b), the activation energy of 1.12 eV is yielded by the linear least-squares fit. In the literature, the $E_a = 2.0$ eV was derived from the low-pressure-grown AlInN [16], which is very close to the In-N bond energy (1.92 eV [17]), suggesting that indium loss is due to the thermal decomposition of InN. However, the smaller activation energy of 1.12 eV for atmospheric-pressure-grown AlInN indicates that indium loss originates from thermal desorption processes that do not involve chemical bond breaking. This is due to the fact that the accelerated mass transport of precursors enhances the adsorption-desorption dynamics of surface atoms at elevated pressures.

3.2. *Influence of precursor flux on in incorporation in growth at atmospheric pressure*

Building upon the analysis of pressure effects, the role of precursor fluxes on In incorporation was further explored under atmospheric pressure.

Fig. 3(a-d) illustrates the evolution of the surface morphology with increasing TMI flux at fixed NH_3 of 8 slm and TMA of 27.0 μmol/min. At low TMI flux, the surface morphology is characterized by unmerged regions accompanied by many voids [Fig. 3(a)]. As the TMI flux increases, these voids gradually diminish [Fig. 3(b)], eventually giving way to a dense and smooth surface [Fig. 3(c)]. At higher flux levels, however, many metallic indium droplets begin to form on the surface [Fig. 3(d)]. In addition, the effects of ammonia on surface morphology at fixed TMI of 129.4 and TMA of 27.0 μmol/min are also exhibited in Fig. 3(e-h). The effect of NH_3 flow rate on the surface morphology [Fig. 3(j)] is similar to that of the variation in TMI flux. In order to gain insight into the incorporation behavior of indium, the In composition is plotted along with the RMS roughness in Fig. 3(i, j). The results of Fig. 3(i) reveal that the In composition initially increases rapidly with increasing TMI flux, while the RMS roughness decreases accordingly due to the reduction of unmerged surface regions, and then both values appear to level off with further increases in TMI flux. At the same TMI flux of about 159.4 μmol/min, the In composition reaches saturation and forms a complete surface morphology accordingly. This behavior suggests that the surface diffusion of adatoms is predominantly governed by In atoms, which is reasonably explained by the fact that the surface mobility of In atoms is much larger than that of Al atoms at the growth temperature of 870 °C. In addition, the effects of ammonia on In incorporation [Fig. 3(j)] also resemble those associated with varying TMI flux, confirming

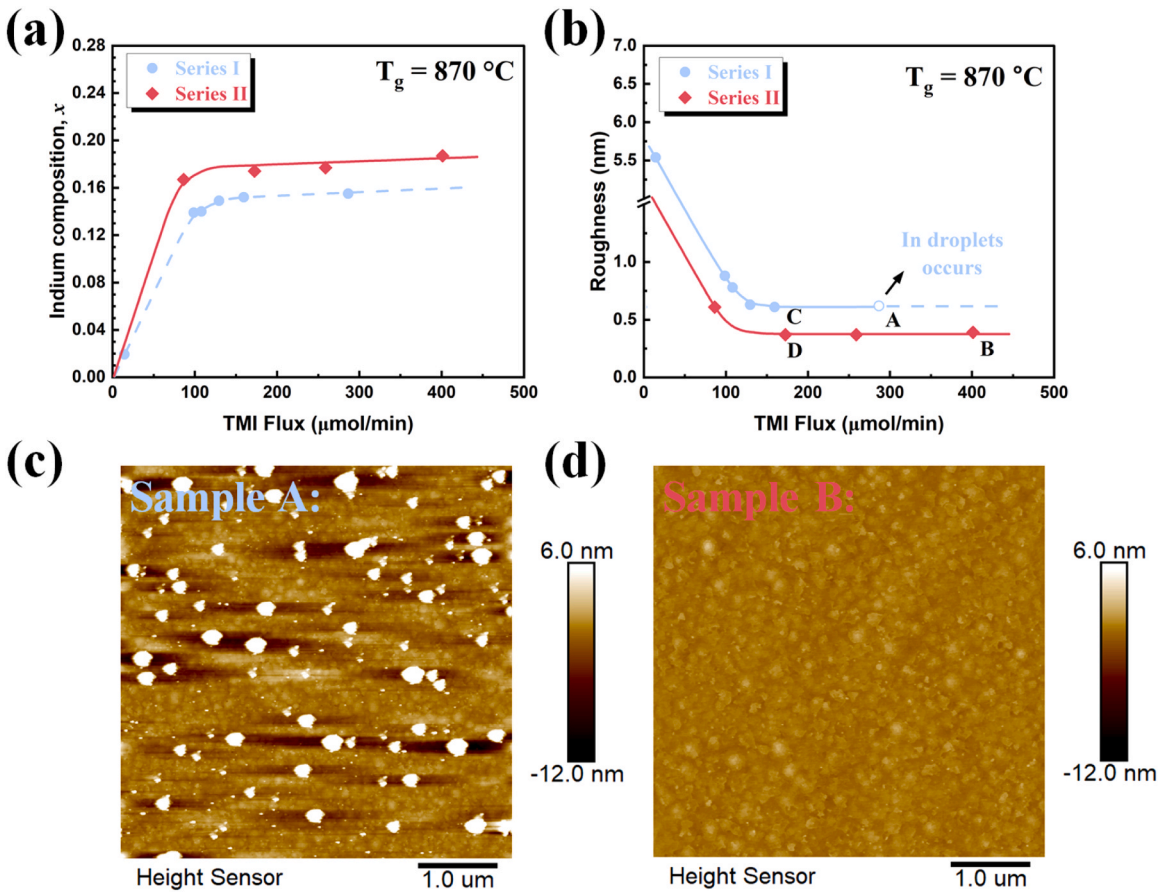

Fig. 5. The dependence of (a) In composition and (b) surface roughness on TMI flux for samples in Series I (blue circles) and Series II (red diamonds). The empty blue circle indicates the roughness at the area without In drops. (c, d) The 5μm × 5μm AFM images of samples A and B.

that elevated NH_3 flow rates enhance indium incorporation efficiency. Its mechanisms will be explained later.

Subsequently, the effect of TMA flux was also investigated. It is worth noting that, as shown in Fig. 4(a), the increase in TMA enhances the growth rate, but simultaneously leads to degradation of surface morphology. This behavior is similar to that observed in AlGaN and is associated with a combination of a high growth rate and the weakened indium surfactant effect [18]. In addition, as shown in Fig. 4(b), the incorporation probability of In relative to Al in the solid, denoted as k_{In}, was calculated using Eq. (2),

$$k_{In} = \frac{x_{In} \bullet [TMA]}{(1 - x_{In}) \bullet [TMI]} \tag{2}$$

Where [*TMA*] and [*TMI*] represent precursor fluxes and x_{In} denotes the In composition.

The incorporation probability of In increases with increasing TMA flux. This may be attributed to the fact that indium incorporation into the Group-III sublattice may be assisted by TMA. Buß *et. al.* previously reported a delayed incorporation behavior of In during AlInN growth, based on carefully designed sample structures and XRD analysis [19]. This delayed incorporation leads to the initial formation of a ~0.4 nm-thick rich aluminum layer. The author explained that the vapor pressure of indium is three orders of magnitude higher than that of aluminum at the ~800 °C temperature region, hindering the effective formation of the indium adsorption layer and following its incorporation. However, the establishment of the rich aluminum layer may maintain the indium adsorption layer by the capping effect, then allow In atoms to incorporate into the lattice to grow AlInN films. A similar observation was made by P. Horenburg *et. al.*, who studied the interfacial compositional dynamics using STEM-EDS maps. Their results showed that indium reaches its nominal composition about 0.35 nm later than aluminum along the growth direction [20]. However, as shown in Fig. 4(c), the TEM-EDX characterization of AlInN grown at atmospheric pressure reveals no such delayed incorporation of In. On the contrary, the In composition reached its stable value even before that of the Al atoms. This difference mainly arises because, under low pressure, Al is more readily incorporated owing to the stronger Al–N bond compared with the In–N bond. As the pressure increases, the residence time of In on the surface becomes longer, thereby enhancing its incorporation probability. In addition, the given TMI flow is much higher than that of TMA, In atoms can even preferentially bond with N atoms and incorporate into the lattice.

3.3. Mechanism of In Incorporation under different precursor supply

The above experimental results demonstrated that both NH_3 and TMA can enhance indium incorporation. In the following section, we provide a quantitative analysis to elucidate their underlying mechanisms. Two sets of samples were designed, named Series I and Series II. The samples in Series I were grown with 12.2 slm of NH_3 and 27 μmol/min of TMA, while the samples of Series II were grown under a higher total gas flow with NH_3 and TMA increased to 34.2 slm and 75.6 μmol/min, respectively.

Fig. 5(a) and Fig. 5(b) show the dependence of In composition and surface roughness on TMI flux for both sample series. It can be observed that, at the same TMI flux level, Series II samples exhibit higher In compositions and smoother surface morphologies, owing to the increased flux of both TMA and NH_3. In contrast, it should be noted from Fig. 4 that an increase in TMA flow alone results in a roughened surface.

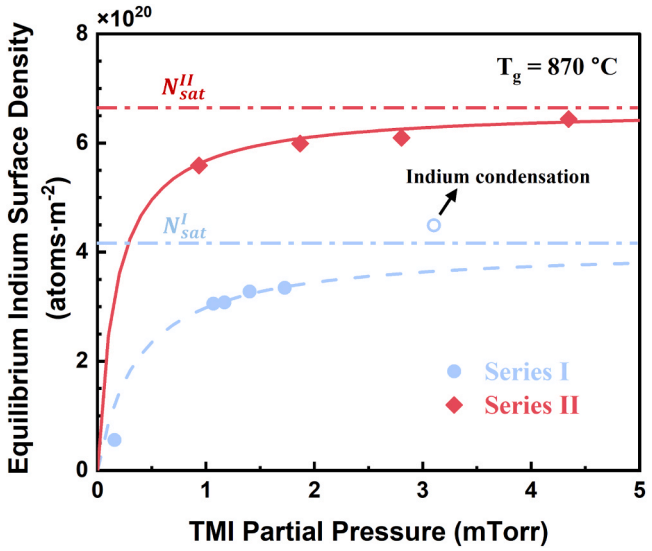

Fig. 6. The TMI partial pressure versus equilibrium indium surface density, together with theory fit using Langmuir model for samples in Series I (blue circles) and Series II (red diamonds).

The degradation at higher TMA is attributed to the enhanced growth rate without sufficient supply of reactive nitrogen atoms. A concurrent increase in NH_3 flow compensates for this deficiency and effectively improves the surface morphology. Finally, for Sample A in series I, when TMI = 286.4 μmol/min, dense metallic In droplets appear on the surface, as shown in Fig. 5(c). Specifically, no droplet formation occurred for Sample B in Series II even at a higher TMI of 401.1 μmol/min (Fig. 5d). This demonstrated that a higher flux of TMA and NH_3 could effectively suppress the formation of indium droplets by facilitating more efficient indium incorporation.

Then, the indium incorporation behaviors observed from Fig. 5(a) can typically be interpreted using the Langmuir model [21]:

$$\frac{dN}{dt} = FS_0\left(1 - \frac{N}{N_{sat}}\right) - \frac{N}{\tau} \tag{3}$$

In this model, the surface density of indium (N) is determined by adsorption (first term) and desorption (second term) processes, and N_{sat} is the saturated surface density of adsorbed indium. For this model, the adsorbed indium atoms block sites for further adsorption, which is reflected in $\left(1 - \frac{N}{N_{sat}}\right)$ item. S_0 is the initial sticking probability on an empty site, and τ is the time constant for indium desorption. F is the supply flux, and is related to the effective indium pressure (P) by $F = P/\sqrt{2\pi mkT}$, where m is the atomic mass of indium and kT is the thermal energy per molecule. P can be expressed by the ratio of the TMI flux to the total incident flows (72 slm) multiplied by the chamber pressure. When equilibrium is achieved, i.e., $dN/dt = 0$, the simplified equilibrium surface density N_{eq}:

$$N_{eq} = N_{sat}P/(P_{eq} + P) \tag{4}$$

The detailed derivation process is provided in the supplementary materials. Here, $P_{eq} = N_{sat} \bullet \sqrt{2\pi mkT}/\tau S_0$ is a fitting parameter, and this can be expressed in terms of the standard free energy of the adsorption reaction, i.e. $P_{eq} = A \bullet \exp(\Delta G^0/kT)$. In this work, it is assumed that S_0 remains constant for all samples, as it primarily depends on the In–N bond energy [22]. Accordingly, the surface density of adsorbed In atoms, N, can be equivalently represented by the surface density of incorporated In atoms in the solid film, which is estimated based on the In composition (x_{In}) and the film thickness (d). For the wurtzite structure, the unit cell volume V_{AlInN} is given by $V_{AlInN} = \frac{\sqrt{3}}{2} \times a^2_{AlInN} \times c_{AlInN}$ with two equivalent group-III atoms per unit cell. Thus, the

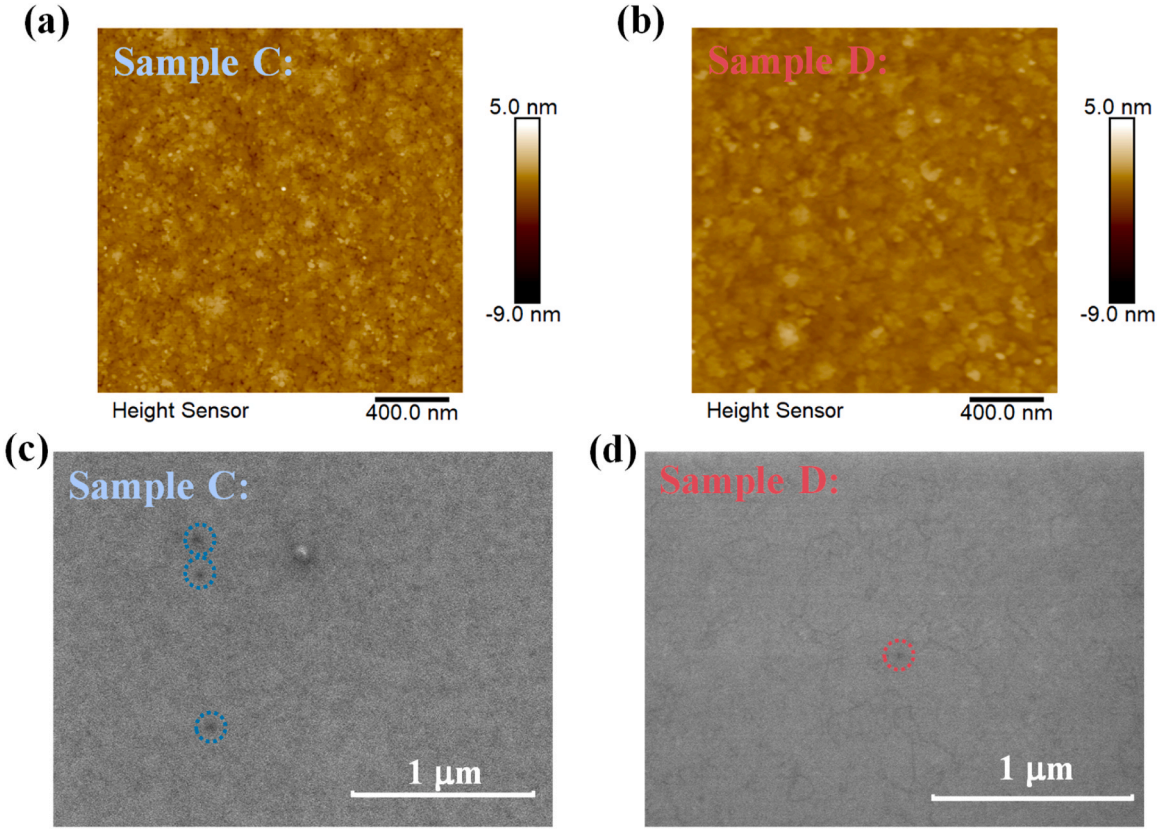

Fig. 7. (a, b) Comparison of the 2μm × 2μm AFM images and (c, d) SEM images of AlInN samples with similar TMI flux, labeled by Sample C and Sample D.

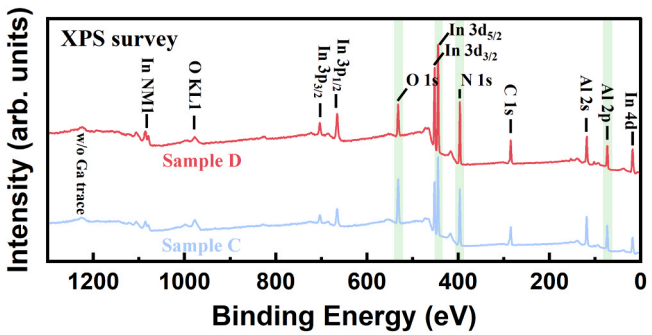

Fig. 8. XPS Survey spectra for AlInN layers grown for Sample C and Sample D grown at a similar TMI flux.

bulk density of Group-III atoms is expressed as $2/V_{AlInN}$, where a_{AlInN} and c_{AlInN} are calculated using the Vegard law. The surface density of incorporated In atoms can then be written as:

$$N_{In} = \frac{2}{V_{AlInN}} \bullet d \bullet x_{In} \tag{5}$$

This model was applied to fit the experimental data, yielding best-fit parameters of P^{I}_{eq} of 0.369 mTorr and N^{I}_{sat} of 4.08×10^{20} atoms/m^2 for the Series I samples, and P^{II}_{eq} of 0.168 mTorr and N^{II}_{sat} of 6.63×10^{20} atoms/m^2 for the Series II samples, as shown in Fig. 6. The lower P^{II}_{eq} indicates that the improved In incorporation is achieved via the suppression of the desorption process by elevated NH_3 and TMA flux. It is worth noting that for Series I, when the TMI Partial Pressure = 3.1 mTorr (as shown by the empty blue circle in Fig. 6), the indium surface density already exceeds the saturation coverage N^{I}_{sat} and thus the excess In atoms are unable to incorporate into the lattice and instead condense on the surface, forming In droplets, in agreement with the AFM image of Fig. 5(c).

3.4. Crystalline quality of AlInN under different precursor supply

To further elucidate the effect of precursor supply on the crystalline quality of AlInN films, two samples grown under both series at the comparable TMI flow rates (referred to as samples C and D in Fig. 5b) were selected for analysis. The surface morphology is investigated on both microscopic and macroscopic scales by AFM and SEM measurements. As shown in Fig. 7(a, b), both surface morphologies exhibit typical morphological features of AlInN films, characterized by densely nanoscale hillocks. For sample C, a large number of nanoscale voids can be observed, which are attributed to the insufficient lateral migration of adatoms resulting from the limited In incorporation. On the other hand, at a larger scale, the SEM image of Sample C shown in Fig. 7(c) reveals a rough, undulating morphology with numerous voids, compared to Sample D [Fig. 7(d)], being consistent with the trend observed in the AFM images.

Next, the chemical states of the AlInN film grown for Sample C and Sample D were analyzed through XPS measurements. The XPS spectra were calibrated using the C 1 s peak (284.6 eV) as a reference binding energy [23]. Fig. 8 shows the complete survey spectrum, indicating the presence of Al, In, N, O, and C elements in the film. Carbon and oxygen impurities probably originated from oxidation on the surface caused by exposure to air. In MOCVD growth of AlInN, some groups observed unwanted gallium incorporation without any intentional gallium supply, resulting in the actual formation of AlInGaN films [24,25]. These Ga may be attributed to both residual Ga-containing precursors from previous growth sequences on the reactor walls or susceptor and the decomposition of preceding Ga-containing layers. However, no clear trace of Ga was detected in our AlInN films, which is attributed to a high total gas flow rate (72 slm) and/or the horizontal MOCVD chamber structure.

Fig. 9 shows the core level spectra for the Al 2p, In $3d_{5/2}$, and N 1 s for both AlInN films. All core levels spectra deconvolution and quantification are performed using a self-consistent peak model [26]. The Al 2p core level spectra of both samples have been deconvoluted into two

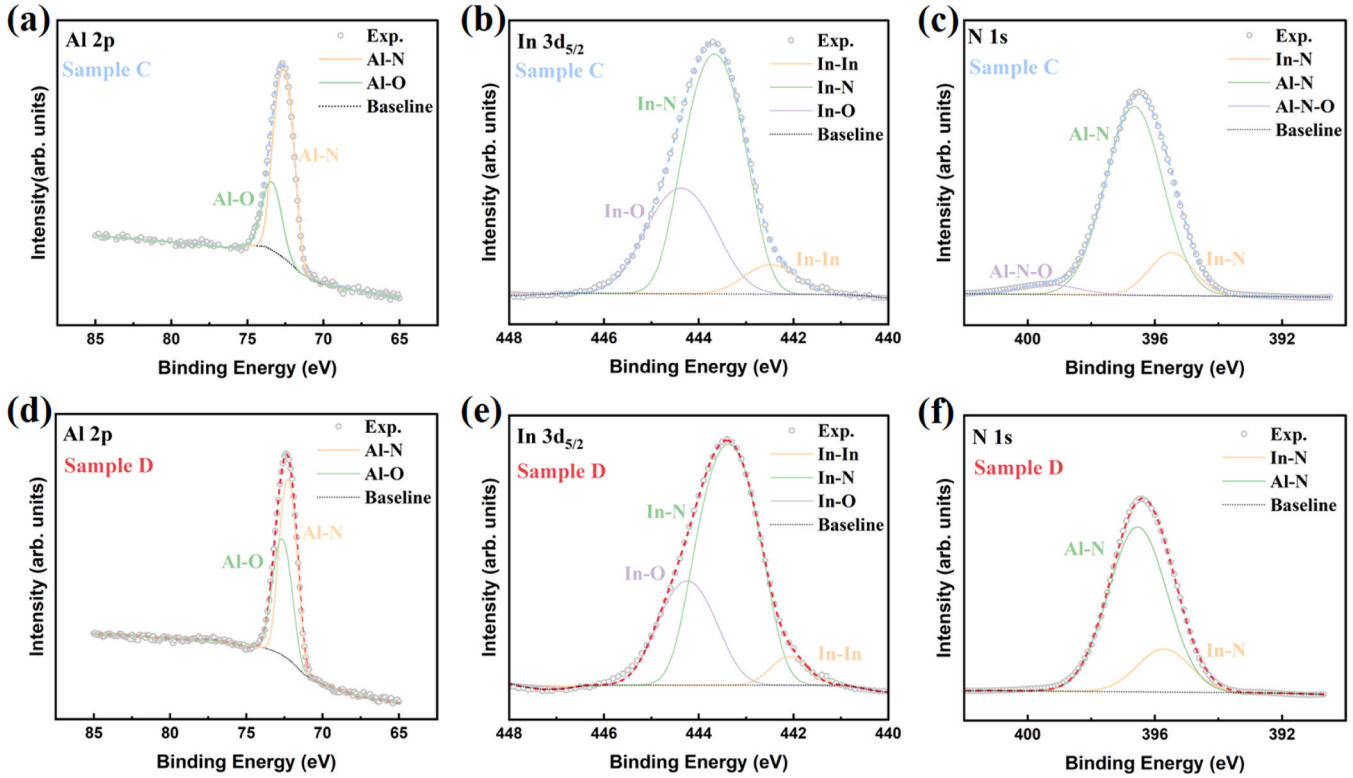

Fig. 9. (a, d) Al2p Signal, (b, e) In3d 5/2 Signal, (c, f) N 1 s core level of Sample C and Sample D, respectively.

Table 1
The percentage of In-related bonds for Sample C and Sample D, as calculated by the peak integrated intensity of In $3d_{5/2}$ core level.

Bonds	Sample C	Sample D
In-O	21.75 %	16.89 %
In-N	74.70 %	80.89 %
In-In	3.55 %	2.22 %

distinct components, which correspond to Al-O and Al-N bonds, respectively. The two photoelectron spectra of In $3d_{5/2}$ are resolved into three main subpeaks, assigned to In-O, In-N, and In-In bonds [27]. The appearance of Al-O and In–O bond indicated the surface oxidation. The synthesis of In-In bonding originates from the accumulation of In atoms on the surface. The synthesis fraction of three In-related chemical bonds is expressed in terms of peak integrated intensity in percentage, as shown in Table 1. In the case of Sample D, the amount of In-In bond is slightly less than that of Sample C, indicating enhanced indium incorporation into lattices. Finally, both of the N 1 s spectra consist of two chemical states, namely Al-N and In-N. The spectra of Sample C exhibit a minor bump at the higher bonding energy side (399.8 eV) corresponding to the Al-N–O bond [28]. However, no such unsatisfied bonds were observed in Sample D. This may be attributed to the fact that more indium atoms can bond with nitrogen with enhanced indium incorporation, thereby reducing the probability of nitrogen bonding with oxygen.

4. Conclusions

In summary, AlInN films were grown at atmospheric pressure and characterized using various experimental and theoretical methods. Compared with low-pressure growth, the incorporation of indium was found to be significantly enhanced under atmospheric pressure conditions. This behavior is attributed to improved adsorption-desorption dynamics, as evidenced by the Arrhenius analysis. Moreover, the addition of TMI, NH_3, and TMA was shown to further promote indium incorporation, primarily by suppressing surface desorption, as proved by the Langmuir model. Notably, a higher TMI and NH_3 flow facilitated indium incorporation while yielding a smoother surface, owing to the larger surface mobility of indium atoms. In contrast, excessive TMA flux, although beneficial for indium incorporation, led to surface degradation, likely due to the growth rate and surfactant effect. Under optimized incorporation conditions, the enhanced incorporation of indium delayed the formation of In droplets and improved surface morphology and crystalline quality.

CRediT authorship contribution statement

Baoping Zhang: Writing – review & editing, Writing – original draft, Supervision, Funding acquisition, Formal analysis, Data curation. **Leiying Ying:** Supervision, Data curation. **Shaosheng Fan:** Writing – review & editing, Writing – original draft, Investigation, Formal analysis, Data curation. **Masao Ikeda:** Supervision, Funding acquisition, Formal analysis, Data curation. **Yang Mei:** Writing – review & editing, Investigation, Data curation. **Ke Xu:** Project administration, Funding acquisition. **Zongliang Liu:** Funding acquisition.

Declaration of Competing Interest

The authors declare that they have no known competing financial interests or personal relationships that could have appeared to influence the work reported in this paper.

Acknowledgments

This work was supported by the National Natural Science Foundation of China (Nos. 62150710548, 62234011, 62474150, and U21A20493) and the National Key Research and Development Program of China (No. 2022YFB3605800), and the Shenzhen Science and Technology Program (No. ZDSYS20220527171201003)

Appendix A. Supporting information

Supplementary data associated with this article can be found in the online version at doi:10.1016/j.jallcom.2025.185078.

Data availability

The data that support the findings of this study are available from the corresponding author upon reasonable request.

References

[1] J.-F. Carlin, M. Ilegems, High-quality AlInN for high index contrast Bragg mirrors lattice matched to GaN, Appl. Phys. Lett. 83 (4) (2003) 668–670, https://doi.org/10.1063/1.1596733.
[2] R. Butté, J.-F. Carlin, E. Feltin, et al., Current status of AlInN layers lattice-matched to GaN for photonics and electronics, J. Phys. D Appl. Phys. 40 (20) (2007) 6328–6344, https://doi.org/0.1088/0022-3727/40/20/S16.
[3] S. Nicolay, J.-F. Carlin, E. Feltin, R. Butté, M. Mosca, N. Grandjean, M. Ilegems, M. Tchernycheva, L. Nevou, F.H. Julien, Midinfrared inter-subband absorption in lattice-matched AlInN/GaN multiple quantum wells, Appl. Phys. Lett. 87 (11) (2005) 111106, https://doi.org/10.1063/1.2045559.
[4] F. Rizzi, K. Bejtka, P.R. Edwards, R.W. Martin, I.M. Watson, Selective wet etching of lattice-matched AlInN–GaN heterostructures, J. Cryst. Growth 300 (1) (2007) 254–258, https://doi.org/10.1016/j.jcrysgro.2006.11.017.
[5] D. Simeonov, E. Feltin, H.-J. Bühlmann, T. Zhu, A. Castiglia, M. Mosca, J.-F. Carlin, R. Butté, N. Grandjean, Blue lasing at room temperature in high quality factor GaN/AlInN microdisks with InGaN quantum wells, Appl. Phys. Lett. 90 (6) (2007) 061106, https://doi.org/10.1063/1.2460234.
[6] T. Matsuoka, Calculation of unstable mixing region in wurtzite $In_{1-x-y}Ga_xAl_yN$, Appl. Phys. Lett. 71 (1) (1997) 105–106, https://doi.org/10.1063/1.119440.
[7] A. Redondo-Cubero, K. Lorenz, R. Gago, N. Franco, M.-A. di Forte Poisson, E. Alves, E. Muñoz, Depth-resolved analysis of spontaneous phase separation in the growth of lattice-matched AlInN, J. Phys. D Appl. Phys. 43 (5) (2010) 055406, https://doi.org/10.1088/0022-3727/43/5/055406.
[8] R.B. Chung, F. Wu, R. Shivaraman, S. Keller, S.P. DenBaars, J.S. Speck, S. Nakamura, Growth study and impurity characterization of $Al_xIn_{1-x}N$ grown by metal organic chemical vapor deposition, J. Cryst. Growth 324 (1) (2011) 163–167, https://doi.org/10.1016/j.jcrysgro.2011.04.025.
[9] H. Kim-Chauveau, P. de Mierry, J.-M. Chauveau, J.-Y. Duboz, The influence of various MOCVD parameters on the growth of $Al_{1-x}In_xN$ ternary alloy on GaN templates, J. Cryst. Growth 316 (1) (2011) 30–36, https://doi.org/10.1016/j.jcrysgro.2010.12.040.
[10] Y. Deng, D.G. Zhao, L.C. Le, D.S. Jiang, L.L. Wu, J.J. Zhu, H. Wang, Z.S. Liu, S. M. Zhang, Hui Yang, J.W. Liang, Relationship between the growth rate and Al incorporation of AlGaN by metalorganic chemical vapor deposition, J. Alloy. Compd. 59 (3) (2011) 748–750, https://doi.org/10.1016/j.jallcom.2010.09.057.
[11] T.C. Sadler, M.J. Kappers, R.A. Oliver, The effect of temperature and ammonia flux on the surface morphology and composition of $In_xAl_{1-x}N$ epitaxial layers, J. Cryst. Growth 311 (13) (2009) 3380–3385, https://doi.org/10.1016/j.jcrysgro.2009.04.004.
[12] T.S. Oh, J.O. Kim, H. Jeong, Y.S. Lee, S. Nagarajan, K.Y. Lim, C.-H. Hong, E.-K. Suh, Growth and properties of Al-rich $In_xAl_{1-x}N$ ternary alloy grown on GaN template by metalorganic chemical vapor deposition, J. Phys. D Appl. Phys. 41 (9) (2008) 095402, https://doi.org/10.1088/0022-3727/41/9/095402.
[13] G. Liu, J. Zhang, X. Li, G. Huang, T. Paskova, K.R. Evans, H. Zhao, N. Tansu, Metalorganic vapor phase epitaxy and characterizations of nearly-lattice-matched AlInN alloys on GaN/sapphire templates and free-standing GaN substrates, J. Cryst. Growth 340 (1) (2012) 66–73, https://doi.org/10.1016/j.jcrysgro.2011.12.037.
[14] S. Fan, M. Ikeda, B. Zhang, Z. Li, X. Su, Z. Liu, K. Xu, Improved surface morphology and reduced V-pits density of lattice-matched AlInN films grown by atmospheric pressure metalorganic chemical vapor deposition, J. Alloy. Compd. 1007 (1) (2024) 176406, https://doi.org/10.1016/j.jallcom.2024.176406.
[15] F. Zhang, M. Ikeda, S. Zhang, J. Liu, A. Tian, P. Wen, Y. Cheng, H. Yang, Thermal etching rate of GaN during MOCVD growth interruption in hydrogen and ammonia ambient determined by AlGaN/GaN superlattice structures, J. Cryst. Growth 475 (2017) 93–96, https://doi.org/10.1016/j.jcrysgro.2017.05.035.
[16] S. Fernández-Garrido, Ž. Gačević, E. Calleja, A comprehensive diagram to grow InAlN alloys by plasma-assisted molecular beam epitaxy, Appl. Phys. Lett. 93 (19) (2008) 191907, https://doi.org/10.1063/1.3026541.
[17] C.S. Gallinat, G. Koblmüller, J.S. Brown, J.S. Speck, A growth diagram for plasma-assisted molecular beam epitaxy of In-face InN, J. Appl. Phys. 102 (6) (2007) 064907, https://doi.org/10.1063/1.2781319.
[18] S. Keller, S. Heikman, I. Ben-Yaacov, L. Shen, S.P. DenBaars, U.K. Mishra, Indium-surfactant-assisted growth of high-mobility AlN/GaN multilayer structures by metalorganic chemical vapor deposition, Appl. Phys. Lett. 79 (21) (2014) 3449, https://doi.org/10.1063/1.1420573.

[19] E.R. Buß, U. Rossow, H. Bremers, A. Hangleiter, Lattice-matched AlInN in the initial stage of growth, Appl. Phys. Lett. 104 (2014) 162104, https://doi.org/10.1063/1.4872226.
[20] P. Horenburg, H. Bremers, R. Imlau, U. Rossow, A. Hangleiter, Microscopic analysis of interface composition dynamics in m-plane AlInN, Jpn. J. Appl. Phys. 58 (SC) (2019) 1008, https://doi.org/10.7567/1347-4065/ab079d.
[21] F. Jiang, R.-V. Wang, A. Munkholm, S.K. Streiffer, G.B. Stephenson, P.H. Fuoss, K. Latifi, Carol Thompson, Indium adsorption on GaN under metal-organic chemical vapor deposition conditions, Appl. Phys. Lett. 89 (16) (2006) 161915, https://doi.org/10.1063/1.2364060.
[22] R. Averbeck, H. Riechert, Quantitative model for the MBE-growth of ternary nitrides, Phys. Stat. Sol. (a) 176 (1) (1999) 301–305, https://doi.org/10.1002/(SICI)1521-396X(199911)176:1<301::AID-PSSA301>3.0.CO;2-H.
[23] M. Alizadeh, V. Ganesh, A. Pandikumar, B.T. Goh, S. Azianty, N.M. Huang, S. A. Rahman, Photoelectrochemical behavior of AlInN thin films grown by plasma-assisted dual source reactive evaporation, J. Alloy. Compd. 670 (2016) 229–238, https://doi.org/10.1016/j.jallcom.2016.02.056.
[24] M.D. SmithE, T.C. Taylor, V.Z. Sadler, K. Zubialevich, H.N. Lorenz, J. Li, E. O'Connell, J.D. Alves, R.W. Holmes, P.J. Martin, Parbrook, Determination of Ga auto-incorporation in nominal InAlN epilayers grown by MOCVD, J. Mater. Chem. C. 2 (2014) 5787–5792, https://doi.org/10.1039/C4TC00480A.
[25] J. Kim, Z. Lochner, M.-H. Ji, S. Choi, H.J. Kim, J.S. Kim, R.D. Dupuis, A.M. Fischer, R. Juday, Y. Huang, T. Li, J.Y. Huang, F.A. Ponce, J.-H. Ryou, Origins of unintentional incorporation of gallium in InAlN layers during epitaxial growth, part II: effects of underlying layers and growth chamber conditions, J. Cryst. Growth 388 (15) (2014) 143–149, https://doi.org/10.1016/j.jcrysgro.2013.09.046.
[26] G. Greczynski, L. Hultman, Self-consistent modelling of X-ray photoelectron spectra from air-exposed polycrystalline TiN thin films, Appl. Surf. Sci. 387 (2016) 294–300, https://doi.org/10.1016/j.apsusc.2016.06.012.
[27] A.N. Hattori, K. Endo, K. Hattori, H. Daimon, Surface treatments toward obtaining clean GaN (0001) from commercial hydride vapor phase epitaxy and metal-organic chemical vapor deposition substrates in ultrahigh vacuum, Appl. Surf. Sci. 256 (2010) 4745–4756.
[28] Wenqing Song, Tao Li, et al., Influence of growth parameters on microstructures and electrical properties of $In_xAl_{1-x}N$ thin films using sputtering, J. Alloy. Compd. 885 (2021) 160977.